

1 **Revision 1**

2 **Cathodoluminescence properties of radiation-induced alkali feldspars**

3

4 **Masahiro Kayama^{1*}, Hirotsugu Nishido², Shin Toyoda³, Kosei Komuro⁴, Adrian A.**

5 **Finch⁵, Martin R. Lee⁶, and Kiyotaka Ninagawa³**

6

7 ¹Department of Earth and Planetary Systems Science, Graduate School of Science,

8 Hiroshima University, Kagami-yama 1-3-1, Higashi-Hiroshima, 739-8526, Japan

9 ²Research Institute of Natural Sciences, Okayama University of Science, 1-1 Ridaicho,

10 Kita-ku, Okayama 700-0005, Japan

11 ³Department of Applied Physics, Okayama University of Science, 1-1 Ridaicho, Kita-ku,

12 Okayama 700-0005, Japan

13 ⁴Earth Evolution Sciences, University of Tsukuba, 1-1-1 Ten-nodai, Tsukuba, 305-8571,

14 Japan

15 ⁵Department of Earth Sciences, University of St Andrews, Irvine Building, North Street,

16 St Andrews, Fife, KY16 9AL, U.K.

17 ⁶School of Geographical and Earth Sciences, University of Glasgow, Lilybank Gardens,

18 Glasgow G12 8QQ, U.K.

19 *Email: kayama27@hiroshima-u.ac.jp

20

21

ABSTRACT

22

23 Cathodoluminescence (CL) spectroscopy provides useful information about the
24 existence of radiation-induced defect centers with a few micrometer resolutions and
25 therefore has great potential to estimate the accumulated dose of natural radiation in
26 micron-ordered mineral grain from radioactive decay. Although great scientific interest
27 exists concerning the CL of various types of minerals, very few investigation have been
28 conducted on the luminescence properties of radiation-induced alkali feldspars. This
29 study, therefore, has sought a clarification of radiation effects on emission centers
30 detected by CL analysis of alkali feldspar implanted with He⁺ ions at 4.0 MeV, which
31 corresponds to the energy of an α particle derived from radioactive decay of ²³⁸U and
32 ²³²Th.

33 Panchromatic CL images of cross-sections of sanidine, orthoclase and microcline show
34 a dark line with ~1 μ m width on the bright luminescent background at 12–15 μ m
35 beneath the implanted surface, of which behavior may be corresponding to the
36 electronic energy loss process of 4.0 MeV He⁺ ion. CL and Raman spectroscopy

37 revealed that He^+ ion implantation may leads to a partial destruction of the feldspar
38 framework and Na^+ migration, resulting in a quenching of CL emission from alkali
39 feldspar, in proportion to the radiation dose. CL spectra of unimplanted and
40 He^+ -ion-implanted sanidine, orthoclase and microcline have emission bands at
41 $\sim 400\text{--}410$ nm and at ~ 730 nm. Deconvolution of the CL spectra can successfully
42 separate these emission bands into emission components at 3.05, 2.81, 2.09, 1.73 and
43 1.68 eV. These components are assigned to the Ti^{4+} impurity, Al-O^- -Al/Ti defect, a
44 radiation-induced defect center, and Fe^{3+} impurities on the T1 and T2 sites, respectively.
45 The intensity at 3.05 eV negatively correlates with radiation dose owing to decreases in
46 the luminescence efficiency. A slight Na^+ diffusion and breaking of the linkage between
47 Ti^{4+} and oxygen as a ligand might reduce the activation energy, which decreases
48 availability of radiative energy in luminescence process of Ti^{4+} impurity center.
49 Furthermore, He^+ ion implantation causes electron holes to be trapped at and released
50 from Löwenstein bridges as a consequence of Na^+ migration and leads to a partial
51 destruction of Al-O bond, which might be responsible for an increase and decrease in
52 the intensity of emission component at 2.81 eV. With an enhanced radiation dose, there
53 is a decrease in intensity at 1.73 eV and an increase in intensity at 1.68 eV.
54 Deconvoluted CL spectra of the alkali feldspars reveal a positive correlation between

55 intensity at 2.09 eV and the radiation dose, which may be due to the formation of a
56 radiation-induced defect center. These correlations can be fitted by an exponential curve,
57 where the gradients differ between the alkali feldspars studied, and are largest for the
58 microcline, followed by the orthoclase and then the sanidine. The intensity at 2.09 eV
59 has the potential to be used in geodosimetry and geochronometry.

60 **Keywords:** cathodoluminescence, alkali feldspar, quenching, radiation-induced defect
61 center, He⁺ ion implantation

62

63

INTRODUCTION

64

65 Luminescence of minerals has been extensively applied in geosciences for
66 geodosimetry and geochronometry (e.g. Smith and Stenstrom 1965; Marshall 1988;
67 Gaft et al. 2005). The accumulated doses of natural radiation that have been
68 accumulated by rock-forming minerals such as quartz and feldspar can be quantitatively
69 estimated using thermoluminescence (TL) and optical stimulated luminescence (OSL)
70 spectroscopy. If the annual dose rate is known, these techniques can then be used to
71 determine the luminescence dating of the minerals in sedimentary rocks and volcanic
72 ejecta. Electron spin resonance (ESR) analysis also enables the detection of lattice

73 defects in minerals, where intensity of ESR from the radiation-induced defect center has
74 been used as an indicator for geodosimetry and geochronometry. It is, however,
75 necessary for estimating the accumulated dose or dating the geological age by TL, OSL
76 and ESR methods to extract a large amount of mineral from the target sediment, so that
77 these techniques are difficult to apply to micrometer sized grains. Cathodoluminescence
78 (CL) spectroscopy also provides useful information about the existence and distribution
79 of radiation-induced defect centers in quartz and feldspar, and with a spatial resolution
80 of a few micrometers (Owen 1988; Komuro et al., 2002; Okumura et al., 2008; Kayama
81 et al. 2011a; Kayama et al. 2011b), suggesting a potential for geodosimetry and
82 geochronometry with respect to a micron-ordered heterogeneous minerals or single
83 grain analysis.

84 The effect of ion implantation on CL emissions from quartz has been investigated to
85 explore the processes whereby radiation-induced defect centers are formed and to
86 estimate the accumulated dose of natural radiation from radioactive decay (e.g. Owen
87 1988; Komuro et al., 2002; Okumura et al., 2008; Krickl et al., 2008; King et al., 2011).
88 According to Komuro et al. (2002) and Okumura et al. (2008), He⁺-ion-implanted
89 quartz at 4.0 MeV shows a bright luminescent band of ~ 14 μm width from the
90 implanted surface as a CL halo, within which the intensity positively correlates with

91 radiation dose. A similar CL halo with $\sim 45 \mu\text{m}$ width from the implanted surface has
92 been also recognized in He^{2+} -ion-implanted quartz and SiO_2 glass at 8.8 MeV, where the
93 intensities increase with radiation dose (Krickl et al., 2008). Although these previous CL
94 studies of ion-implanted quartz have demonstrated a good correspondence between CL
95 intensity and radiation dose, the dose response to ion implantation differs between
96 quartz samples of various origins, suggesting that the use of CL of quartz in
97 geodosimetry is not straightforward. Okumura et al. (2008) concluded that the CL
98 intensity of quartz depends on not only the radiation dose, but also other factors such as
99 density of defect centers (e.g., $[\text{AlO}_4/\text{M}^+]^0$ defect, self-trapped exciton, non-bridging
100 oxygen hole centers) and on the concentration of impurity centers (e.g., Ge^{4+} and Fe^{3+}
101 impurities). Accordingly, further work is required to elucidate how CL of
102 radiation-induced quartz can be used in geodosimetry.

103 CL has also been used to detect radiation-induced defect centers in He^+ -ion-implanted
104 albite (Kayama et al. 2011a; Kayama et al., 2011b). In this case, radiation resulted in a
105 characteristic red emission, whose intensity increased with radiation dose.
106 Deconvolution of CL spectra by Gaussian fitting revealed an emission component at
107 1.861 eV that was assigned to a radiation-induced defect center produced by He^+ ion
108 implantation. No investigations of ion implantation on the CL properties of alkali

109 feldspars (e.g. sanidine, orthoclase and microcline) have been performed. Most alkali
110 feldspars show a blue CL emission assigned to Al-O⁻-Al defect center, and the intensity
111 depends on the natural radiation dose (Finch and Klein, 1999). Ion implantation
112 corresponding to α particle radiation, therefore, potentially affects the CL emissions
113 assigned to Al-O⁻-Al defect centers as well as other emission centers such as Ti⁴⁺ and
114 Fe³⁺ impurities, which should be interpreted in detail for the application of CL to
115 geodosimetry and geochronometry.

116 In this study, CL of He⁺-ion-implanted alkali feldspars at 4.0 MeV, corresponding to
117 energy of α particle from radioactive decay of ²³⁸U and ²³²Th, was measured to clarify
118 the effect of ion implantation on luminescent emissions derived from defect and
119 impurity centers. Raman spectroscopy was also conducted for the implanted alkali
120 feldspar to investigate a formation process of radiation-induced defect centers produced
121 by He⁺ ion implantation.

122

123

SAMPLES AND METHODS

124

125 CL and Raman analyses were carried out for unimplanted and He⁺-ion-implanted
126 samples of single crystals of sanidine (Sa) (Or₈₇Ab₁₃) phenocrysts from syenite and

127 phonolite xenoliths in Quaternary diatreme from Eifel, Germany, microperthitic
128 orthoclase (Or) ($\text{Or}_{93}\text{Ab}_7$) from Late Variscan granite in the Karlovy Vary Massif from
129 Karlovy Vary, Czech Republic and microperthitic microcline (Mi) ($\text{Or}_{89}\text{Ab}_{11}$) as
130 pegmatite minerals from Naegi granite in Late Cretaceous Sanyo-type granitic zone
131 from Nakatsugawa, Gifu, Japan. These alkali feldspars were identified by X-ray
132 diffraction analysis. Microstructures and microtextures associated with exsolution,
133 micropores and twinning were located by optical microscopy and backscattered electron
134 SEM imaging of the plagioclase grains and avoid in subsequent CL work owing to their
135 potential impact on the results. The sliced samples ($10 \times 10 \times 1$ mm) were cut
136 perpendicular to c-axis for CL and Raman measurements in order to avoid a polarization
137 effects as suggested by Finch et al. (2003). The sliced samples were polished and
138 finished with a 1 μm diamond abrasive. CL microscopy and spectroscopy were
139 preliminarily conducted on the surface of the sliced samples to select the areas with
140 comparable CL intensity and homogeneous distribution of the intensity before the He⁺
141 ion implantation experiments.

142 He⁺ ion implantation was conducted perpendicular to their surface using a 3M-tandem
143 ion accelerator located at Takasaki Research Center of the Japan Atomic Energy
144 Research Institute. The ion-beam condition had a 4.0 MeV implantation energy,

145 corresponding to the energy of alpha particles from ^{238}U and ^{232}Th disintegrations,
146 where a specific dose density was set in the range from 2.18×10^{-6} to 6.33×10^{-4} C/cm²
147 for the sanidine and 4.83×10^{-6} to 4.64×10^{-4} C/cm² for the orthoclase and microcline
148 (Table 1). The implanted samples for sanidine, orthoclase and microcline were
149 numbered in order of dose density, e.g., Sa00 for unimplanted sanidine and Sa10 for the
150 highest dose. CL spectra were acquired from the implanted surface of the samples,
151 which is indicated by the postscript “S”, e.g., Or01S for orthoclase implanted at the
152 lowest dose and Or08S for oligoclase implanted at the highest dose. The implanted
153 samples were also cut perpendicular to their exposed surface to enable CL line analysis
154 and high-resolution CL imaging of the surface in cross-section. The sectional samples
155 are denoted by the postscript “C”, e.g., Mi00C for unimplanted microcline and Mi10C
156 for microcline implanted at the highest radiation dose. Further details of the He⁺ ion
157 implantation experiment and sample preparation can be found in Okumura et al. (2008)
158 and Kayama et al. (2011a).

159 A scanning electron microscopy-cathodoluminescence (SEM-CL) instrument was
160 carried out using a JEOL: JSM-5410 SEM combined with a grating monochromator
161 (Oxford: Mono CL2) to measure CL spectra. All CL spectra obtained in the range from
162 300 to 800 nm in 1 nm steps were corrected for the total instrumental response, which

163 was determined using a calibrated standard lamp. CL line analysis was measured across
164 a profile from He⁺ ion implanted surface (0 μm) to a depth of 20 μm with 0.25 μm steps,
165 where the bulk intensity of the panchromatic CL (300 to 800 nm) was obtained. The
166 operating conditions were set as follows: an accelerating voltage of 15 kV and a beam
167 current of 2.0 nA in scanning mode with a 220 × 185 μm scanning area, which was
168 established based on the preliminary CL spectroscopy for prevention of electron
169 irradiation damage and enhancement of the signal/noise (S/N) ratio. According to
170 Kayama et al. (2010), the corrected CL spectra in energy units were deconvoluted into
171 the Gaussian components corresponding to each emission center using the peak-fitting
172 software (Peak Analyzer) implemented in OriginPro 8J SR2. Peak position and integral
173 intensity of the Gaussian component were acquired from each five deconvoluted CL
174 spectra of unimplanted and He⁺ ion-implanted sanidine, orthoclase and microcline at
175 different radiation dose. High-resolution CL images were obtained using the Gatan:
176 MiniCL imaging system under the same condition as CL spectral analysis by SEM-CL.
177 More details of the equipment construction and analytical procedures are in Ikenaga et
178 al. (2000) and Kayama et al. (2010).

179 A laser Raman microscope (Thermo Electron; Nicolet: Almega XR) was used for
180 Raman spectral measurements, where the Nd:YAG laser (532 nm excitation line) was

181 selected and controlled at 20 mW with a $\sim 1 \mu\text{m}$ spot size. The operating conditions were
182 set as five accumulations of 10 s each in the range 120 to 900 cm^{-1} in steps of 1 cm^{-1} .
183 Raman bands were calibrated by monitoring the position of the O-Si-O stretching
184 vibration (464 cm^{-1}) in reference to a standard high optical grade quartz before and after
185 the measurements. Details of instrument construction and analytical procedures can
186 found in Kayama et al. (2009).

187

188 **RESULTS**

189

190 **CL microscopy**

191

192 Panchromatic CL images of cross-sections of sanidine implanted at $3.03 \times 10^{-4} \text{ C/cm}^2$
193 (Sa09C) and of orthoclase (Or08C) and microcline (Mi08C) both implanted at $4.64 \times$
194 10^{-4} C/cm^2 show a dark line with $\sim 1 \mu\text{m}$ width on the bright luminescent background at
195 12–15 μm beneath the implanted surface (Fig. 1). Similar dark lines occur in CL images
196 of all other implanted samples, but they are absent from unimplanted alkali feldspars.
197 The reduction in CL intensity that produces the dark line is more obvious for high dose
198 than low dose implanted samples. Optical microscopy, and secondary electron (SE), and

199 backscattered electron (BSE) imaging reveal no microstructures or textures
200 corresponding to the dark line observed in the CL image (Fig. 1).

201

202 **CL line analysis**

203

204 CL line analyses were carried out on cross-sections of Sa09C, Or08C and Mi08C (Fig.
205 2). The analysis line is shown in Fig. 1, and extends from the implanted surface to a
206 depth of 20 μm , which includes the dark line at 12–15 μm . CL intensities of Sa09C
207 appear to slightly decrease with the implantation depth, show a drastic drop at 12–15
208 μm , then increase to 16 μm (Fig. 2). Similar changes in intensity were found in CL line
209 analyses of other sanidine cross-section samples. All implanted orthoclase and
210 microcline samples also show similar depth-dependent change in CL intensities (Fig. 2).

211

212 **CL spectroscopy**

213

214 CL spectra of unimplanted sanidine (Sa00S) and microcline (Mi00S) have emission
215 bands in the blue (~410 nm) and red-IR regions (~730 nm) (Figs. 3a and c). A UV
216 emission at ~320 nm also occurs in the spectrum of Mi00S, and the intensity of this

217 peak is appreciably lower than of the emission bands in the blue and red-IR regions (Fig.
218 3c). Unimplanted orthoclase (Or00S) has similar UV, blue and red-IR emission with
219 higher intensities than Sa00S and Mi00S. CL spectroscopy of Sa09S reveals emission
220 bands at ~410 and ~730 nm, similar to those of Sa00S, whereas CL intensity of the blue
221 emission in Sa09S is lower than in Sa00S (Fig. 3a). Also, CL of Sa09S exhibits a
222 yellow-orange emission from 550 to 600 nm overlapped and concealed by the blue and
223 red-IR emissions. The intensity of the yellow-orange emission increases with the
224 radiation dose. CL spectra of Or08 and Mi08 consist of emission bands at ~320 nm in
225 the UV, ~410 nm in the blue and ~730 nm in the red-IR regions, and these spectral
226 patterns are similar to unimplanted orthoclase and microcline (Figs. 3b and c). The
227 implanted orthoclase and microcline show a decrease in the blue emission intensities
228 and an increase in the yellow-orange ones with an increase in radiation dose.

229

230 **Raman spectroscopy**

231

232 Raman spectra of unimplanted sanidine, orthoclase and microcline have pronounced
233 peaks at ~160, ~285, ~455, ~480 and ~515 cm^{-1} , and weak ones at ~360, ~405, ~750
234 and ~810 cm^{-1} . Similar peaks are also observed in Raman spectra of dark line areas at

235 12–15 μm depth in Sa09C, Or08C and Mi08C, which have lower intensities, larger
236 bandwidths and high background compared to those of unimplanted samples. Raman
237 line analyses of Sa09C, Or08C and Mi08C that were obtained from the implanted
238 surface to the inside with 20 μm depth reveal that the integral-peak intensities at 515
239 cm^{-1} slightly decrease at 12–15 μm depth, then increase with greater depth (Fig. 4).

240

241

DISCUSSION

242

243 **Characteristics of CL on implanted surface**

244

245 Panchromatic CL images of the cross-sections show a dark line at 12–15 μm beneath
246 the implanted surface (Fig. 1), and this distance is close to the maximum of electronic
247 energy loss ($\sim 12.5 \mu\text{m}$) of 4.0 MeV He^+ ion in alkali feldspars (Bragg and Kleeman
248 1905; Nogami and Hurley 1948; Faul 1954; Owen 1988; Komuro et al., 2002; Okumura
249 et al., 2008). By monochromatic CL imaging, Kayama et al. (2011a) found a similar
250 dark line beneath the implanted surface of albite, again, corresponding to the range of
251 He^+ ion implantation at 4.0 MeV. CL line analyses acquired through the cross-sections
252 of all implanted alkali feldspars also reveal decreases in emission intensities at 12–15

253 μm (Fig. 2). However, the distance at 12–15 μm is not completely concordant with the
254 maximum of electric energy loss process, which may be due to He^+ ion implantation
255 condition or spatial resolution of CL microscopy proposed by Okumura et al. (2008).
256 Nevertheless, it is noteworthy that He^+ ion implantation definitely make a quench of CL
257 emission from alkali feldspar around the end of the ion track, in proportion to the
258 radiation dose.

259 Raman spectra acquired from the dark line in CL imaging of Sa09, Or08 and Mi08
260 are of a lower peak intensity, broader bandwidth and high background than those seen in
261 unimplanted samples. Raman line analyses of Sa09C, Or08C and Mi08C show a slight
262 decrease in the integral-peak intensity at 515 cm^{-1} in the dark line at 12–15 μm ,
263 assigned to T-O stretch and O-T-O deformation modes in TO_4 group (Fig. 4) (von
264 Stengel 1977; Freedman et al. 2003). A similar phenomenon has been recognized in the
265 Raman spectra of He^+ -ion-implanted albite (Kayama et al., 2011a; Kayama et al.,
266 2011b). These facts imply that He^+ ion implantation may destroy the linkage between
267 TO_4 tetrahedra or induce a strain, and consequently quenches CL in alkali feldspar. This
268 has been also observed in zircon, where the luminescence and Raman intensity is
269 reduced in proportion to metamictization (Nasdala et al. 2002; Kempe et al. 2010).

270 According to the previous studies, ion implantation also results in the migration of

271 monovalent cations in alkali feldspar. Monovalent cations such as Na^+ migrate in the
272 lattice of feldspar during Pb ion implantation (Petit et al., 1987). The extent of lattice
273 damage caused by ion implantation and its consequent diffusion are determined by the
274 implantation dose (Watson and Dohmen 2010). According to Jambon and Carron (1976),
275 diffusion coefficient of alkali element in feldspar may depend on the defect density.
276 Lineweaver (1963) demonstrated that electron irradiation transfers alkali elements into
277 unirradiated areas due to formation of the electric fields produced by defection of
278 oxygen. Although the cation migration potentially occurs in associated with ion
279 implantation, it may be slight effective because there is almost no difference of Na^+
280 content, obtained from chemical analysis by wavelength dispersive X-ray spectroscopy
281 (WDS), between unimplanted and the implanted alkali feldspars. Taken together these
282 findings indicate that the partial destruction, introduction of strain and the slight Na^+
283 migration due to He^+ ion implantation may be the cause of quenching of CL in alkali
284 feldspar rather than the Na^+ migration. This CL quenching may be responsible for a
285 conversion of emission center related to the present alkali feldspar into non-luminescent
286 center due to an alteration of the energy state or a change of luminescence efficiency
287 due to a variation of the activation energy, as will be described in the section of
288 "Radiation effects on each emission center".

289 With an increase in the radiation dose on alkali feldspars, emission intensities of blue
290 CL decrease sharply, whereas yellow-orange emissions intensities increase and red-IR
291 intensities slightly decrease or increase depending on the samples (Fig. 3). This pattern
292 indicates that He⁺ ion implantation effect on CL vary depending on type of emission
293 center. Although CL line analysis reveals a decrease in the intensity at 12–15 μm caused
294 by an elimination of the emission center due to the partial destruction, introduction of
295 strain or the Na⁺ migration, there should also be an accumulation of radiation-induced
296 defect centers related to the brightening CL emission around the end of the ion track.
297 Therefore, CL halo in feldspars may be produced and characterized by both elimination
298 and creation of the emission centers due to radiation, where the former should be the
299 dominant process for the present alkali feldspar with the dark line and the later should
300 be for albite with bright luminescent band reported by Kayama et al. (2011a).

301

302 **Assignment of emission centers**

303

304 The blue emission at 400–410 nm, shown in Fig. 3, is assigned to the following
305 centers; (1) an oxygen defect associated with the electron hole trapped Löwenstein
306 bridge (Al-O⁻-Al defect center) formed with two Al atoms, one of which is structural Al

307 and the others is impurity Al (Marfunin 1979; Finch and Klein 1999; Götze et al. 2000;
308 Slaby et al. 2008; Kayama et al. 2010) and (2) Ti^{4+} incorporated with Al sites, which act
309 as impurity center and/or oxygen defect associated with Al-O-Ti bridges (Marfunin and
310 Bershov 1970; Mariano et al. 1973; Mariano and Ring 1975; Speit and Lehmann 1976;
311 Kirsh et al. 1987; Smith and Brown 1988; Ginibre et al. 2004; Lee et al. 2007; Parsons
312 et al. 2008; Kayama et al. 2010). According to Kayama et al. (2010), the blue emission
313 band consists of an overlap of two components, namely the oxygen defect centers
314 associated with Al-O-Al and Al-O-Ti bridges (Al-O⁻-Al/Ti defect center) and the Ti^{4+}
315 impurity center. The alkali feldspars also have the red-IR CL emission attributed to a
316 Fe^{3+} impurity that substitutes for Al^{3+} ions in tetrahedral sites for the luminescence
317 caused by the radiative transition of the electrons from 4T_1 to 6A_1 (Telfer and Walker
318 1978; Finch and Klein 1999; Götze et al. 2000). Kayama et al. (2010) clarified the
319 suggestion of Finch and Klein (1999) that the red-IR CL emission is composed of two
320 components assigned to Fe^{3+} impurity centers on T1 and T2.

321 CL spectra of the implanted alkali feldspars have yellow-orange emission from 550 to
322 600 nm (Fig. 3), of which intensities increase with radiation dose. Ionoluminescence
323 (IL) spectrum of alkali feldspar shows a similar increase in the intensity depending on
324 the radiation dose (Brooks et al. 2002). A comparable increase in the CL intensity with

325 radiation dose has been also observed in red emissions from He⁺-ion-implanted albite,
326 which is characteristic of the radiation-induced defect center (Kayama et al. 2011a;
327 Kayama et al. 2011b). Krickl et al. (2008) also demonstrated a similar yellow emission
328 assigned to the radiation-induced defect center in He²⁺ irradiated natural and synthetic
329 SiO₂ phase as well as natural α -quartz with radiohaloes. This suggests the formation of
330 radiation-induced defect center in alkali feldspar by He⁺ ion implantation and/or change
331 in quantum efficiency of the recombination site.

332 According to deconvolution method suggested by Stevens-Kalceff (2009) and Kayama
333 et al. (2010), the emission bands in CL spectra from the sanidine, orthoclase and
334 microcline can be separated into five Gaussian components, at 3.05, 2.81, 2.09, 1.73 and
335 1.68 eV, where their peak position and integral intensity are obtained from each five
336 deconvoluted CL spectral of unimplanted and the implanted alkali feldspar at different
337 radiation dose. The emission components at 3.05 and 2.81 eV are constituents of the
338 emission bands in the blue spectral region, where the former is assigned to Ti⁴⁺ impurity
339 center and the latter to Al-O⁻-Al/Ti defect center (Kayama et al. 2010). The red-IR
340 emission comprises the components at 1.73 and 1.68 eV that Kayama et al. (2010)
341 attributes to the Fe³⁺ impurity centers on the T1 and T2 sites, respectively. Intensity of
342 the component at 2.09 eV increases with radiation dose, implying a characteristic CL

343 signal of the radiation-induced defect center (Fig. 5). The emission component assigned
344 to the radiation-induced defect center is also detectable in the deconvoluted CL spectra
345 of He⁺-ion-implanted albite, but the peak wavelength (1.861 eV) is distinct from that
346 obtained from the alkali feldspar in the present study (2.09 eV). According to Blasse
347 and Grabmaier (1994), Götze et al. (2000) and Stevens-Kalceff et al. (2000), the peak
348 position of an emission band varies with chemical composition, crystal structure in host
349 lattice, and type of emission center. Therefore, further studies such as annealing
350 experiment and ESR analysis will be necessary for an identification of type of
351 radiation-induced defect center.

352

353 **Radiation effects on each emission center**

354

355 Figures 6, 7, 8 and 9 plot intensities of Gaussian components at 3.05 eV, 2.81 eV, 2.09
356 eV, 1.73 eV and 1.68 eV against dose density of He⁺ ion implantation on the sanidine,
357 orthoclase and microcline, where the averaged intensities and the standard deviations
358 are obtained from five deconvoluted CL spectra of each of these feldspar implanted at
359 respective radiation dose. They elucidate radiation effects on CL of alkali feldspar
360 activated by each emission center, as follows.

361

362 **Ti⁴⁺ impurity center**

363

364 Intensities of the emission component at 3.05 eV decrease sharply with increasing
365 radiation doses up to 1.07×10^{-4} C/cm² for sanidine and 9.42×10^{-5} C/cm² for
366 orthoclase and microcline, then decrease more gradually above that threshold. As
367 described above, He⁺ ion implantation potentially leads to the partial destruction,
368 introduction of strain and the slight Na⁺ migration in the alkali feldspars judging from
369 the present results obtained by Raman spectroscopy and EPMA analysis and the
370 previous studies, which may be responsible for quenching of the CL activated by Ti⁴⁺
371 impurity center. According to Brooks et al. (2001), ion implantation reduces activation
372 energy associated with hopping between adjacent channels, which is a function of the
373 luminescence efficiency (Curie 1963). Kayama et al. (2009) demonstrated that the
374 activation energy depends on the structural state in SiO₂ polymorphs, which may be due
375 to a change of the energy state in host. Therefore, luminescence efficiency as well as the
376 activation energy varies depending on the structural state in the host, as suggested by
377 Blasse and Grabmaier (1994). A change of the structural state by partial destruction,
378 introduction of strain or the Na⁺ migration during He⁺ ion implantation may decrease a

379 luminescence efficiency of Ti^{4+} impurity center in the alkali feldspars due to a change in
380 the activation energy. Alternatively, it may lead to an alteration of the energy state in
381 Ti^{4+} impurity center, resulting in a conversion of the emission center into
382 non-luminescent center. Nevertheless, these outcomes of these processes may quench
383 the blue CL in alkali feldspars. The energy used as CL activated by the Ti^{4+} impurity
384 center might be transferred into lattice vibration as phonon, or applied for radiative
385 transition of the electron at other emission centers. However, further works will be
386 necessary to validate an adequacy of this model.

387

388 **Al-O⁻-Al/Ti defect center**

389

390 The emission components at 2.81 eV increase in intensity with an increase in low
391 radiation level of He^+ ion for sanidine and microcline (Figs. 6b and 8b). IL spectroscopy
392 of alkali feldspar also revealed an increase in the blue emission intensity with the
393 radiation dose, which may be due to a formation of defect or vacancy in the structure
394 (Brooks et al. 2002). Finch and Klein (1999) modeled the CL intensity of the blue
395 emission in feldspar scales with the percentage of Löwenstein bridges with electron
396 holes (Al-O⁻-Al defect center) in the structure, which is closely related to natural

397 radiation dose received by the feldspar during its geological history. ESR analysis
398 demonstrated that electron holes at oxygen positions (e.g., Al-O⁻-Al) in feldspars are
399 produced by natural gamma ray and X-ray radiation (Petrov et al., 1989). Furthermore,
400 the diffusion of monovalent cations in quartz in response to ion implantation converts
401 the [AlO₄/M⁺]⁰ defect (M: H⁺, Li⁺, Na⁺ and K⁺) into the [AlO₄]⁰ defect (equivalent to
402 the Al-O⁻-Al defect in feldspar), resulting in an increase in the blue emission intensity
403 with elevated radiation doses (King et al., 2011). Electron holes may be derived from
404 the slight Na⁺ migration in sanidine and microcline with He⁺ ion implantation and
405 subsequently trapped in Löwenstein bridges in various extents depending on the
406 radiation dose, which might be responsible for an increase in the blue CL intensity at
407 relatively low radiation level.

408 The intensities at 2.81 eV, however, decrease with as a function of radiation dose up to
409 $2.41 \times 10^{-5} \text{ C/cm}^2$ for orthoclase (Fig. 7b). The emission intensity is substantially higher
410 in unimplanted orthoclase than unimplanted sanidine and microcline (Fig. 6, 7 and 8),
411 which, taking the Finch and Klein (1999) model at face value, implies that the
412 orthoclase may have quite high percentage of Löwenstein bridges with electron holes.
413 The sanidine at $1.07 \times 10^{-4} \text{ C/cm}^2$ and the microcline at $9.42 \times 10^{-5} \text{ C/cm}^2$ have a
414 maximum intensity at 2.81 eV in Figure 6b and 8b, implying their sufficient high

415 percentage of Löwenstein bridges. Electron holes, therefore, may have been already
416 trapped in almost all Löwenstein bridges in the orthoclase before He^+ ion implantation
417 and in the sanidine and microcline after the implantation at relatively high radiation
418 dose, which may contribute to no increase in the intensity at 2.81 eV for the orthoclase
419 as well as the implanted sanidine and microcline at high level of radiation dose.
420 According to King et al. (2011), a mobility of an electron in quartz by ion implantation
421 also changes $[\text{AlO}_4]^0$ defect into $[\text{AlO}_4]^-$ defect, where the former acts as emission
422 center, but latter as non-luminescent center. Al-O⁻-Al/Ti defect centers in the orthoclase,
423 and the implanted sanidine and microcline at relatively high radiation dose might be
424 eliminated and converted into non-luminescent centers due to the Na^+ migration by He^+
425 ion implantation, which quenches their blue CL. Furthermore, Raman spectroscopy
426 shows a slight decrease in the integral-peak intensity at 515 cm^{-1} in the dark lines.
427 Radiation dose leads to a breaking of many Al-O bond in framework structure of the
428 alkali feldspar and then eliminating a large amount of Al-O⁻-Al/Ti defect centers. An
429 introduction of strain of AlO_4 tetrahedra due to He^+ ion implantation may be also due to
430 a change of the energy state in Al-O⁻-Al/Ti defect centers. These processes might be
431 also responsible for the quenching effect on the blue CL.
432

433 **Fe³⁺ impurity center**

434

435 The radiation doses on sanidine up to 1.07×10^{-4} C/cm² decrease the intensity of
436 emission components at 1.73 eV assigned to the Fe³⁺ impurity center on T1 sites. This
437 effect is also seen to doses of up to 9.42×10^{-5} C/cm² for the microcline. The
438 component at 1.68 eV, which is the Fe³⁺ impurity center on T2 sites, increases in
439 intensity with the radiation dose up to 1.07×10^{-4} C/cm² in sanidine, 4.83×10^{-5} C/cm²
440 in orthoclase and 2.50×10^{-4} C/cm² in microcline (Figs. 6, 7 and 8). This may
441 contribute to an energy transition between Fe³⁺ impurity centers on T1 and T2 sites.
442 The minimal partial destruction, introduction of strain or slight Na⁺ migration may
443 cause a decrease in the luminescence efficiency of Fe³⁺ impurity center on T1 site as a
444 consequence of a change of activation energy or a conversion of the emission center
445 into non-luminescent center by an alteration of the energy state, the same as in the case
446 of Ti⁴⁺ impurity center. Consequently, the red-IR CL in alkali feldspar may be quenched
447 by these processes derived from He⁺ ion implantation. These results are concordant with
448 IL spectral data of Fe³⁺-activated emission obtained from alkali feldspar (Brooks et al.
449 2002). A part of energy for luminescence emission from the Fe³⁺ impurity center on the
450 T1 site should be consumed by radiative transition of Fe³⁺ impurity center on T2 site as

451 the energy transition process, resulting in an enhancement of the red-IR CL intensity.
452 The rate of increase of emission intensity at 1.68 eV is lower for orthoclase than for
453 sanidine and microcline (Figs. 6c, 7c and 8c). This may be due to the low concentration
454 of Fe³⁺ impurity centers on the T1 site judging from undetectable emission component
455 at 1.73 eV in orthoclase, although further works will be necessary for an establishment
456 of this model.

457 The emission component at 1.68 eV in sanidine shows a decrease in the intensity with
458 an increase in the radiation dose above 1.07×10^{-4} C/cm² (Fig. 6c). According to
459 Kayama et al. (2009), a change in framework configuration by partial destruction of its
460 structure alters the emission centers into non-luminescent centers with consequent
461 quenching of CL due to an increase in the population of non-radiative transition. This is
462 observed in other mineral systems, for example, Nasdala et al., (2002) demonstrated
463 that natural radiation destroys the structure of zircon, leading to a decrease in emission
464 intensity depending on the radiation dose. These facts indicate that the linkages between
465 the Fe³⁺ ions on T2 site and oxygen as their ligands might be appreciably broken or
466 strained by He⁺ ion implantation at relatively high radiation dose, and consequently the
467 emission center is converted into non-luminescent center. Similarly, such change of the
468 energy state of the emission center should be caused by the slight Na⁺ migration, which

469 also results in a quenching of CL activated by Fe^{3+} impurity centers on the T2 site. On
470 the other hand, the intensities at 1.68 eV for orthoclase and microcline increase with
471 radiation dose up to $4.64 \times 10^{-4} \text{ C/cm}^2$ and reach a the saturation level above $4.83 \times$
472 10^{-5} C/cm^2 for orthoclase and $2.50 \times 10^{-4} \text{ C/cm}^2$ for microcline. Since Raman
473 spectroscopy indicates that the framework of the disordered feldspar appears to be more
474 prone to damage than ordered feldspar (Fig. 4), He^+ ion implantation effects of the
475 structure-breaking may be potentially exerted to the sanidine rather than the orthoclase
476 and microcline. Most Fe^{3+} impurity centers on the T2 site act as an emission center in
477 orthoclase and microcline, but not in the sanidine at relatively high radiation dose,
478 which might explain the lack of a decrease in intensity at 1.68 eV in the orthoclase and
479 microcline with the enhanced radiation dose.

480

481 **Radiation-induced defect center**

482

483 The emission components at 2.09 eV exponentially increase in intensity with radiation
484 dose in the low radiation level, although the gradients differ between the alkali feldspars,
485 and are largest for the microcline, followed by the orthoclase and then the sanidine (Fig.
486 9). Saturation of the intensity is reached at $4.02 \times 10^{-6} \text{ C/cm}^2$ for sanidine, above $2.41 \times$

487 10^{-5} C/cm² for orthoclase and above 4.83×10^{-5} C/cm² for microcline; the saturated
488 intensity of the ordered alkali feldspar tends to be higher than that of the disordered one.
489 This pattern implies that an increase in the CL intensity of the yellow-orange emission
490 assigned to the radiation-induced defect center might be closely related to the degree of
491 Si-Al order. ESR studies on feldspar have also demonstrated that signals attributed to
492 oxygen vacancies linked between Si and Al tetrahedra vary depending on natural
493 gamma and X-ray radiation doses and the degree of Si-Al ordering (Matyash et al.,
494 1982; Petrov et al., 1989). The emission component at 2.09 eV in the alkali feldspar,
495 therefore, might be assigned to one or more of the oxygen vacancy centers. Further
496 investigations such as annealing experiment and ESR analysis of radiation-induced
497 alkali feldspars will allow us to specify type of the oxygen vacancy centers.

498 Figure 9 reveals that there is no decrease in the intensity at 2.09 eV with the enhanced
499 radiation dose up to 6.33×10^{-4} C/cm² for sanidine and up to 4.64×10^{-4} C/cm² for the
500 orthoclase and microcline. The components at 2.81 eV, however, decrease sharply in
501 intensity in the range of relatively high radiation doses, which might be due to breaking
502 of Al-O bonds related to the Al-O⁻-Al/Ti defect center by He⁺ ion implantation. These
503 results indicate that formation of the radiation-induced defect center assigned to
504 component at 2.09 eV in the alkali feldspar should be a dominant process rather than an

505 elimination of the center due to the partial breaking of the structure in the present range
506 of the radiation dose.

507 The dose response of intensity at 2.09 eV appears to be mainly controlled only by the
508 degree of Si-Al ordering, even though other properties including chemical composition,
509 crystal structure, concentration and distribution of other emission centers and the
510 presence of microstructures or microtextures also differ between the alkali feldspars.
511 Kayama et al. (2011b) demonstrated that several albite from different localities show
512 almost same dose response of the intensity at 1.86 eV, not depending on other properties
513 of these albite crystals. In the case of alkali feldspar, therefore, a quantitative estimation
514 of α radiation dose from natural radionuclides using the intensity at 2.09 eV requires a
515 correction for the CL spectral data on the basis of the degree of Si-Al ordering, but
516 probably not to other mineralogical features. Eventually, the intensity at 2.09 eV may be
517 used as an indicator for geodosimetry, and then geochronometry based on the additive
518 dose method, which provide progressive application in geoscience and planetary science,
519 e.g. clarification of space weathering on lunar regolith and micron-order grain recovered
520 from Itokawa asteroid, sedimentary dating in wide applicable range, estimation of
521 leakage of nuclear waste from geologic disposal facilities and atomic power plant.

522

523

ACKNOWLEDGMENTS

524

525 We are deeply indebted to Dr. S. Nakano (Shiga University, Shiga, Japan) for helpful
526 suggestions on CL of feldspar. We thank Dr. Y. Shibata (Technical center, Hiroshima
527 University, Hiroshima, Japan) for technical support on WDS using EPMA. The
528 measurement of EPMA was made using JXA-8200 at the Natural Science Center for
529 Basic Research and Development (N-BARD), Hiroshima University. We also appreciate
530 Dr. J. Götze (TU Bergakademie Freiberg, Freiberg, Germany) for his careful reading
531 and valuable suggestions on luminescence of radiation-induced minerals, which led to
532 improvements in the manuscript. He⁺ ion implantation experiments were supported by
533 the Inter-University Program for the Joint Use of the Japan Atomic Energy Agency
534 (Takasaki), grant No. 21010 to H. N.

535

536

REFERENCES

537

538 Blasse, G. and Grabmaier, B.C. (1994) Radiative return to the ground state: Emission. In
539 Luminescent Materials, 52, chapter 3, p. 33–70. Springer Verlag, Berlin.
540 Bragg, W. H., and Kleman, R. (1905) Alpha particles or radium, and their loss of range

- 541 passing through various atoms and molecules. *Philosophical Magazine*, 10, 318–334.
- 542 Brooks, R. J., Ramachandran, V., Hole, D. E., Townsend, P. D. (2001) Dose rate effects
543 in ion beam luminescence. *Radiation Effects and Defects in Solids: Incorporating*
544 *Plasma Science and Plasma Technology*, 155, 177–181.
- 545 Brooks, R. J., Finch, A. A., Hole, D. E., Townsend, P. D., and Wu, Z. (2002) The red to
546 near-infrared luminescence in alkali feldspar. *Contributions to Mineralogy and*
547 *Petrology*, 143, 484–494.
- 548 Curie, D. (1963) Thermal and optical activation of trapped electrons: Quenching effects.
549 In *Luminescence in Crystals*, chapter 7, p. 202–208. Methuen and Co. Ltd., London.
- 550 Faul, H. (1954) *Nuclear geology*, John Wiley (New York), 414.
- 551 Freeman, J. J., Wang, A., Kuebler, K. E., and Haskin, L. A. (2003) Raman spectroscopic
552 characterization of the feldspars-Implications for in situ surface mineral characterization
553 in planetary exploration. *Lunar and Planetary Science XXXIV*, 1676.
- 554 Finch, A. A., and Klein, J. (1999) The causes and petrological significance of
555 cathodoluminescence emission from alkali feldspars. *Contributions to Mineralogy and*
556 *Petrology*, 135, 234–243.
- 557 Finch, A. A., Hole, D. E., and Townsend, P. D. (2003) Orientation dependence of
558 luminescence in plagioclase. *Physics and Chemistry of Minerals*, 30, 373–381.

- 559 Gaft, M., Reisfeld, R., and Panczer, G. (2005) Luminescence Spectroscopy of Minerals
560 and Materials, Springer-Verlag (Berlin), 52.
- 561 Götze, J., Krbetschek, M.R., Habermann, D., and Wold, D. (2000) High-resolution
562 cathodoluminescence of feldspar minerals. In M. Pagel, V. Barbin, P. Blanc, and D.
563 Ohnenstetter, Eds., Cathodoluminescence, p. 245–270. Geosciences, Springer Verlag,
564 Berlin.
- 565 Ginibre, C., Wörner, G., and Kronz, A. (2004) Structure and dynamics of the Laacher
566 see magma chamber (Eifel, Germany) from major and trace element zoning in sanidine:
567 A cathodoluminescence and electron microprobe study. *Journal of Petrology*, 45,
568 2197–2223.
- 569 Ikenaga, M., Nishido, H., and Ninagawa, K. (2000) Performance and analytical
570 conditions of cathodoluminescence scanning electron microscope (CL-SEM). *The*
571 *Bulletin of Research Institute of Natural Sciences Okayama University of Science*, 26,
572 61–75.
- 573 Jambon, A., and Carron, J. P. (1976) Diffusion of Na, K, Rb and Cs in glasses of albite
574 and orthoclase composition. *Geochimica et Cosmochimica Acta*, 40, 897–903.
- 575 Kayama, M., Nishido, H., and Ninagawa, K. (2009) Cathodoluminescence
576 characterization of tridymite and cristobalite: Effects of electron irradiation and sample

- 577 temperature. *American Mineralogist*, 94, 1018–1028.
- 578 Kayama, M., Nakano, S., and Nishido, H. (2010) Characteristics of emission centers in
579 alkali feldspar: A new approach by using cathodoluminescence spectral deconvolution.
580 *American Mineralogist*, 95, 1783–1795.
- 581 Kayama, M., Nishido, H., Toyoda, S., Komuro, K., and Ninagawa, K. (2011a) Radiation
582 effects on cathodoluminescence of albite, *American Mineralogist*, 96, 1238–1247.
- 583 Kayama, M., Nishido, H., Toyoda, S., Komuro, K., and Ninagawa, K. (2011b)
584 Combined Cathodoluminescence and Micro-Raman Study of Helium-Ion-Implanted
585 Albite. *Spectroscopy Letters*, 44, 526–529.
- 586 Kempe, U., Thomas, S-M., Geipel, G., Thomas, R., Plötze, M., Böttcher, R. Grambole,
587 G., Hoentsch, J., and Trinkler, M. (2010) Optical absorption, luminescence, and electron
588 paramagnetic resonance (EPR) spectroscopy of crystalline to metamict zircon: Evidence
589 for formation of uranyl, manganese, and other optically active centers. *American*
590 *Mineralogist*, 95, 335–347.
- 591 King, G. E., Finch, A. A., Robinson, R. A. J., and Hole, D. E. (2011) The problem of
592 dating quartz 1: Spectroscopic ionoluminescence of dose dependence. *Radiation*
593 *Measurements*, 46, 1–9.
- 594 Kirsh, Y., Shoval, S., and Townsend, P.D. (1987) Kinetics and emission spectra of

- 595 thermoluminescence in the feldspar albite and microcline. *Physica status solidi (a)*, 101,
596 253–262.
- 597 Komuro, K., Horikawa, Y., and Toyoda, S. (2002) Development of radiation-damage
598 halos in low-quartz: cathodoluminescence measurement after He⁺ ion implantation.
599 *Mineralogy and Petrology*, 76, 261–266.
- 600 Krickl, R., Nasdala, L., Götze, J., Grambole, D., and Wirth, R. (2008) Alpha-irradiation
601 effects in SiO₂. *European Journal of Mineralogy*, 20, 517–522.
- 602 Lee, M. R., Parsons, I., Edwards, P. R., and Martin, R. W. (2007) Identification of
603 cathodoluminescence activators in zoned alkali feldspars by hyperspectral imaging and
604 electron-probe microanalysis. *American Mineralogist*, 92, 243–253.
- 605 Marfunin, A. S. (1979) *Spectroscopy, luminescence and radiation centers in minerals*.
606 Springer-Verlag (Berlin), 352.
- 607 Marfunin, A.S. and Bershov, L.V. (1970) Electron-hole centers in feldspars and their
608 possible crystalchemical and petrological significance. *Doklady Akademii Nauk*, 193,
609 412–414.
- 610 Mariano, A.N. and Ring, P.J. (1975) Europium-activated cathodoluminescence in
611 minerals. *Geochimica et Cosmochimica Acta*, 56, 175–185.
- 612 Mariano, A. N., Ito, J., and Ring, P. J. (1973) Cathodoluminescence of plagioclase

- 613 feldspars. Geological Society of America, Abstract Program, 5, 726.
- 614 Marshall, D. J. (1988) Cathodoluminescence of Geological Materials. Hyman (Boston),
615 146.
- 616 Matyash, V. I., Bagmut, N. N., Litovchenko, C. A., and Proshko, Ya. V. (1982) Electron
617 paramagnetic resonance study of new paramagnetic centers in microcline-perthites from
618 pegmatites. Physics and Chemistry of Minerals, 8, 149–152.
- 619 McKeown, D. A. (2005) Raman spectroscopy and vibrational analyses of albite: From
620 25 °C through the melting temperature. American Mineralogist, 90, 1506–1517.
- 621 Nasdala, L., Lengauer, C. L., Hanchar, J. M., Kronz, A., Wirth, R., Blanc, P., Kennedy,
622 A. K., and Seydoux-Guikkaume, A. M. (2002) Annealing radiation damage and the
623 recovery of cathodoluminescence, Chemical Geology, 191, 121–140.
- 624 Nogami, H., and Hurley, P. M. (1948) The absorption factor in counting alpha rays from
625 thick mineral sources. American Geophysical Union Transactions, 29, 335–340.
- 626 Okumura, T., Nishido, H., Toyoda, S., Kaneko, T., Kosugi, S., and Sawada, Y. (2008)
627 Evaluation of radiation-damage halos in quartz by cathodoluminescence as a
628 geochronological tool. Quaternary Geochronology, 3, 342–345.
- 629 Owen, M. R. (1988) Radiation-damage halos in quartz. Geology, 16, 529–532.
- 630 Parsons, I., Steele, D. A., Lee, M. R., and Magee, C. W. (2008) Titanium as a

- 631 cathodoluminescence activator in alkali feldspar. *American Mineralogist*, 93, 875–879.
- 632 Perny, B., Eberhardt, P., Ramseyer, K., Mullis, J., and Pankrath, R. (1992)
633 Microdistribution of Al, Li, and Na in α -quartz: Possible causes and correlation with
634 short-lived cathodoluminescence. *American Mineralogist*, 77, 534–544.
- 635 Petit, J. C., Dran, J. C., and Della Mea, G. (1987) Effects of ion implantation on the
636 dissolution of minerals. In Part II. Selective dissolution. *Bulletin de Minéralogie*, 110,
637 25–42.
- 638 Petrov, I., Agel, A., and Hafner, S. S. (1989) Distinct defect centers at oxygen positions
639 in albite. *American Mineralogist*, 74, 1130–1141.
- 640 Slaby, E., Götze, J., Simon, K., and Wörner, G. (2008) K-feldspar phenocrysts in
641 microgranular magmatic enclaves: Cathodoluminescence and geochemical studies on
642 crystal growth as a marker of magma mingling dynamics. *Lithos*, 105, 85–97.
- 643 Smith, J.V. and Brown, W.L. (1988) *Feldspar Minerals. 1. Crystal structures, physical,*
644 *chemical, and microtextural properties*, 828 p. Springer-Verlag, Berlin.
- 645 Smith, J. V., and Stenstrom, R. C. (1965) Electron-excited luminescence as a petrologic
646 tool. *Journal of Geology*, 73, 627–635.
- 647 Speit, B. and Lehmann, G. (1976) Hole centers in the feldspar sanidine. *Physica status*
648 *solidi (a)*, 36, 471–481.

- 649 Stengel, M. O. von (1977) Normalschwingungen von Alkalifeldspäten. Zeitschrift für
650 Kristallographie, 146, 1–18.
- 651 Stevens-Kalceff, M. A. (2009) Cathodoluminescence microcharacterization of point
652 defect in α -quartz. Mineralogical Magazine, 73, 585–605.
- 653 Stevens-Kalceff, M. A., Matthew, R. P., Anthony, R. M., and Kalceff, W. (2000)
654 Cathodoluminescence microcharacterisation of silicon dioxide polymorphs. In M. Pagel,
655 V. Barbin, P. Blanc, and D. Ohnenstetter, Eds., Cathodoluminescence in Geosciences,
656 chapter 8, p. 193–223. Springer, Berlin.
- 657 Telfer, D.J., and Walker, G. (1978) Ligand field bands of Mn^{2+} and Fe^{3+} luminescence
658 centers and their site occupancy in plagioclase feldspar. Modern Geology, 6, 199–210.
- 659 Watson, E. B., and Dohmen, R. (2010) Non-traditional Emerging Methods for
660 Characterizing Diffusion in Minerals and Mineral Aggregates. In Y. Zhang, and D. J.
661 Cherniak, Eds., Reviews in Mineralogy & Geochemistry. Mineralogical Society of
662 America Geochemical Society, p. 61–105.

663

664

FIGURE AND TABLE CAPTION

665

666 **Figure 1.** (a) Panchromatic CL image of a cross-section of He^+ -ion-implanted (a)

667 sanidine (Sa09C), (b) orthoclase (Or08C) and (c) microcline (Mc08C). White lines
668 indicate trace of CL and Raman line analyses for the alkali feldspars, shown in Figures
669 2a and 4d . Scale bars are 20 μm .

670

671 **Figure 2.** Plot of the relationship of CL emission intensity over the 300–800 nm range
672 obtained by CL line analysis from the He^+ -ion-implanted surface to 20 μm . The samples
673 analyzed are Sa09C, Or08 and Mi08. The path of the line analysis is indicated by the
674 white lines in Figure 1.

675

676 **Figure 3.** CL spectra of (a) unimplanted (Sa00S) and He^+ -ion-implanted sanidine
677 (Sa09S), (b) unimplanted (Or00S) and He^+ -ion-implanted orthoclase (Or08S), and (c)
678 unimplanted microcline (Mi00S) and He^+ -ion-implanted microcline (Mi08S).

679

680 **Figure 4.** Plot showing the change in intensity of the Raman peak at 515 cm^{-1} from the
681 implanted surfaces of cross-section samples of Sa09C, Or08C and Mi08C to 20 μm
682 depth. A slight decrease in the intensity at 515 cm^{-1} is observed at $\sim 10\text{ }\mu\text{m}$, which is
683 responsible for the cracks. Measured areas of the Raman line analysis are indicated in
684 Fig. 1 as white lines.

685

686 **Figure 5.** Deconvolution of CL spectra in energy units obtained from
687 He⁺-ion-implanted (a) sanidine (Sa09S), (b) orthoclase (Or08S) and microcline (Mi08S).
688 Data are fitted by several Gaussian curves.

689

690 **Figure 6.** A plot of the intensity of the Gaussian component at 2.09 eV obtained using
691 CL spectral deconvolution against dose density of He⁺ ion implantation for the sanidine
692 (Sa00S to Sa10S), orthoclase (Or00S to Or08S) and microcline (Mi00S to Mi08S).

693

694 **Figure 7.** Plots of intensities of Gaussian components at (a) 3.05 eV, (b) 2.81 eV, (c)
695 1.68 eV and (d) 1.73 eV obtained using CL spectral deconvolution for the sanidine
696 (Sa00S to Sa10S) against dose density of He⁺ ion implantation.

697

698 **Figure 8.** Plots of intensities of Gaussian components at (a) 3.05 eV, (b) 2.81 eV and (c)
699 1.68 eV obtained using CL spectral deconvolution for the orthoclase (Or00S to Or08S)
700 against dose density of He⁺ ion implantation.

701

702 **Figure 9.** Plots of intensities of Gaussian components at (a) 3.05 eV, (b) 2.81 eV, (c)

703 1.68 eV and (d) 1.73 eV obtained using CL spectral deconvolution for the microcline
704 (Mi00S to Mi08S) against dose density of He⁺ ion implantation..

705

706 **Table 1.** Samples of alkali feldspars for CL and Raman measurements.

707

No.	Dose density (C/cm ²)	No.	Dose density (C/cm ²)
Sa00	Unimplanted	Or00 Mi00	Unimplanted
Sa01	2.18×10^{-6}	Or01 Mi01	4.83×10^{-6}
Sa02	4.02×10^{-6}	Or02 Mi02	9.65×10^{-6}
Sa03	2.54×10^{-5}	Or03 Mi03	2.41×10^{-5}
Sa04	6.97×10^{-5}	Or04 Mi04	4.83×10^{-5}
Sa05	1.07×10^{-4}	Or05 Mi05	9.42×10^{-5}
Sa06	1.19×10^{-4}	Or06 Mi06	1.77×10^{-4}
Sa07	1.40×10^{-4}	Or07 Mi07	2.32×10^{-4}
Sa08	1.49×10^{-4}	Or08 Mi08	4.64×10^{-4}
Sa09	3.03×10^{-4}		
Sa10	6.33×10^{-4}		

Sa, Or and Mi indicate sanidine, orthoclase and microcline, respectively.

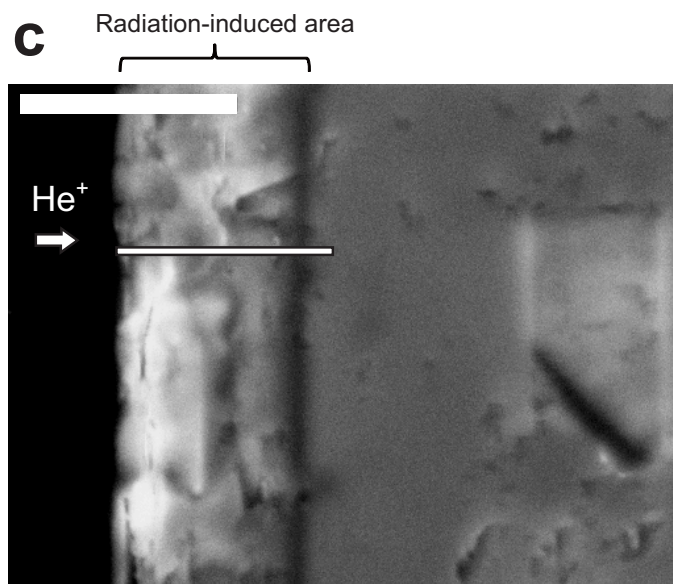
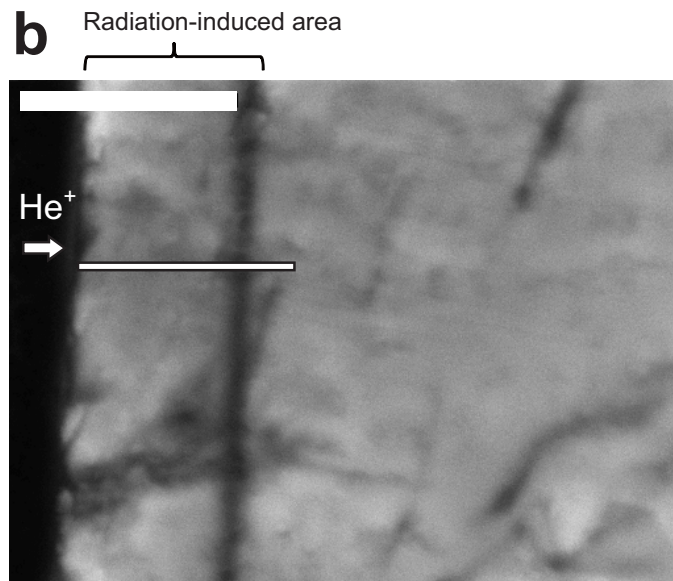
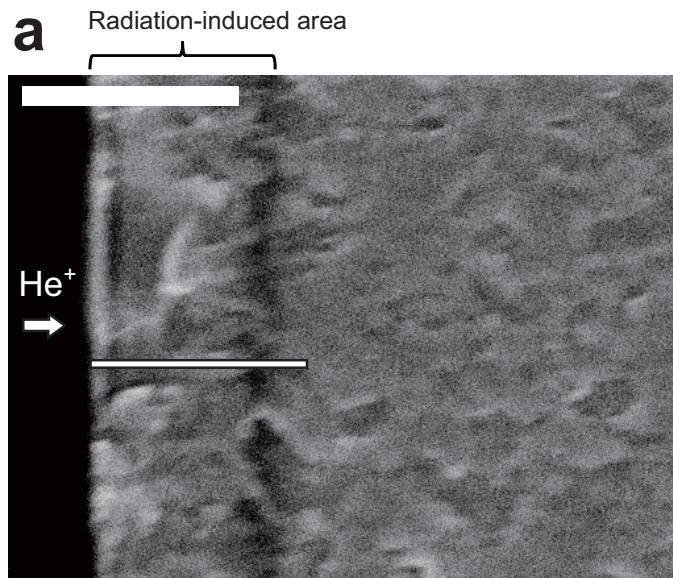


Figure 1

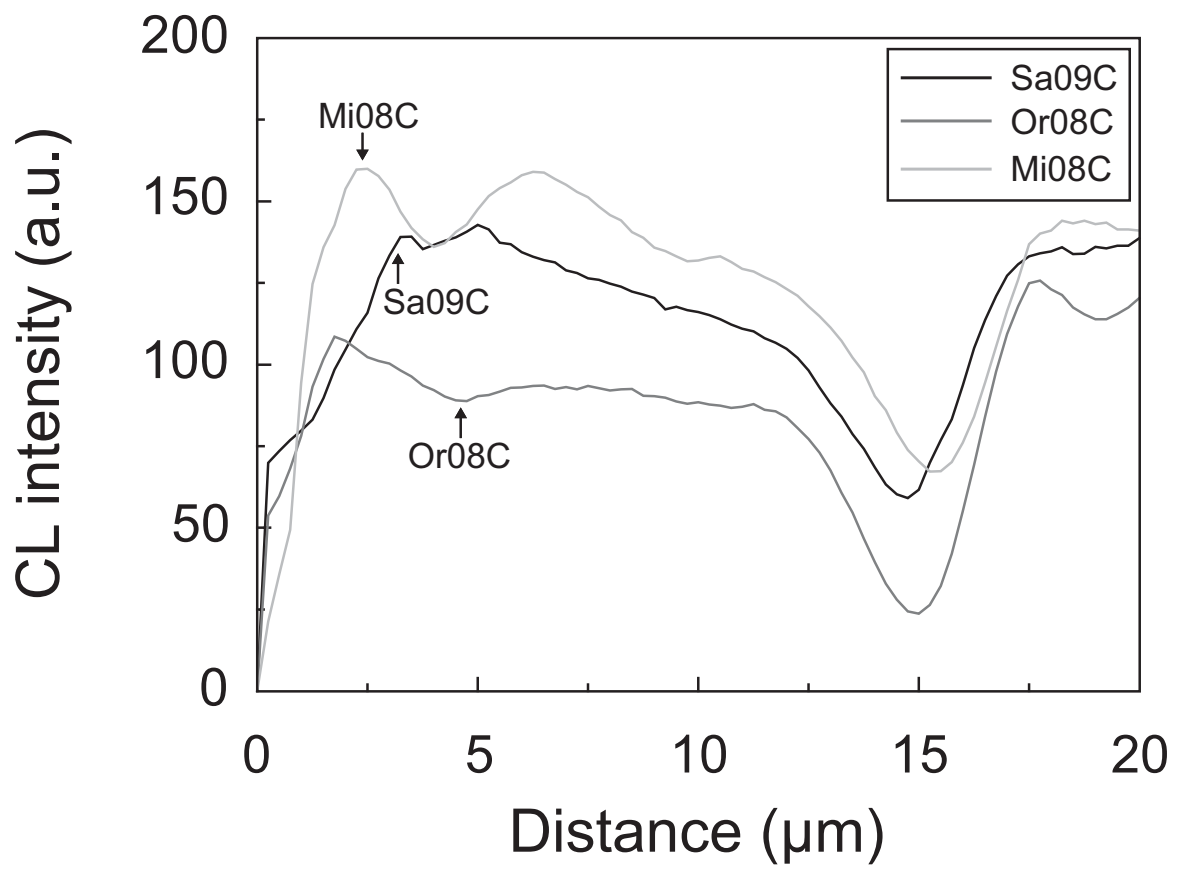


Figure 2

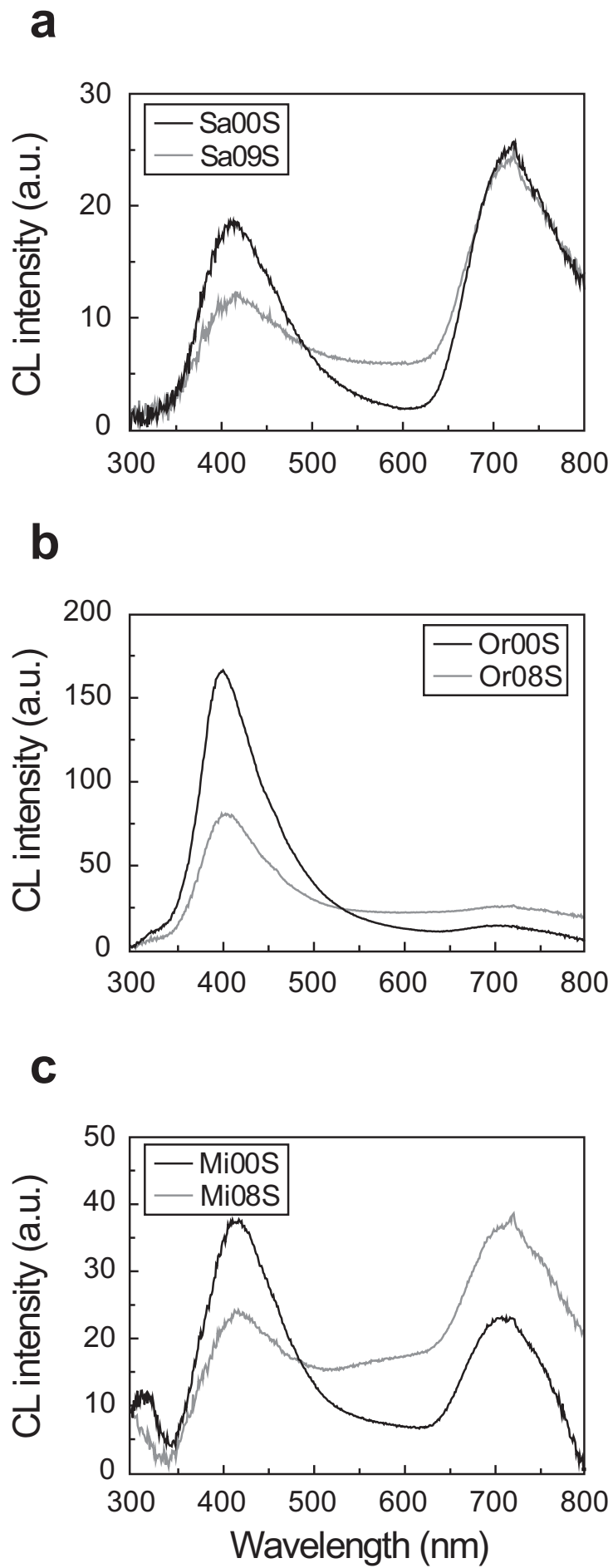


Figure 3

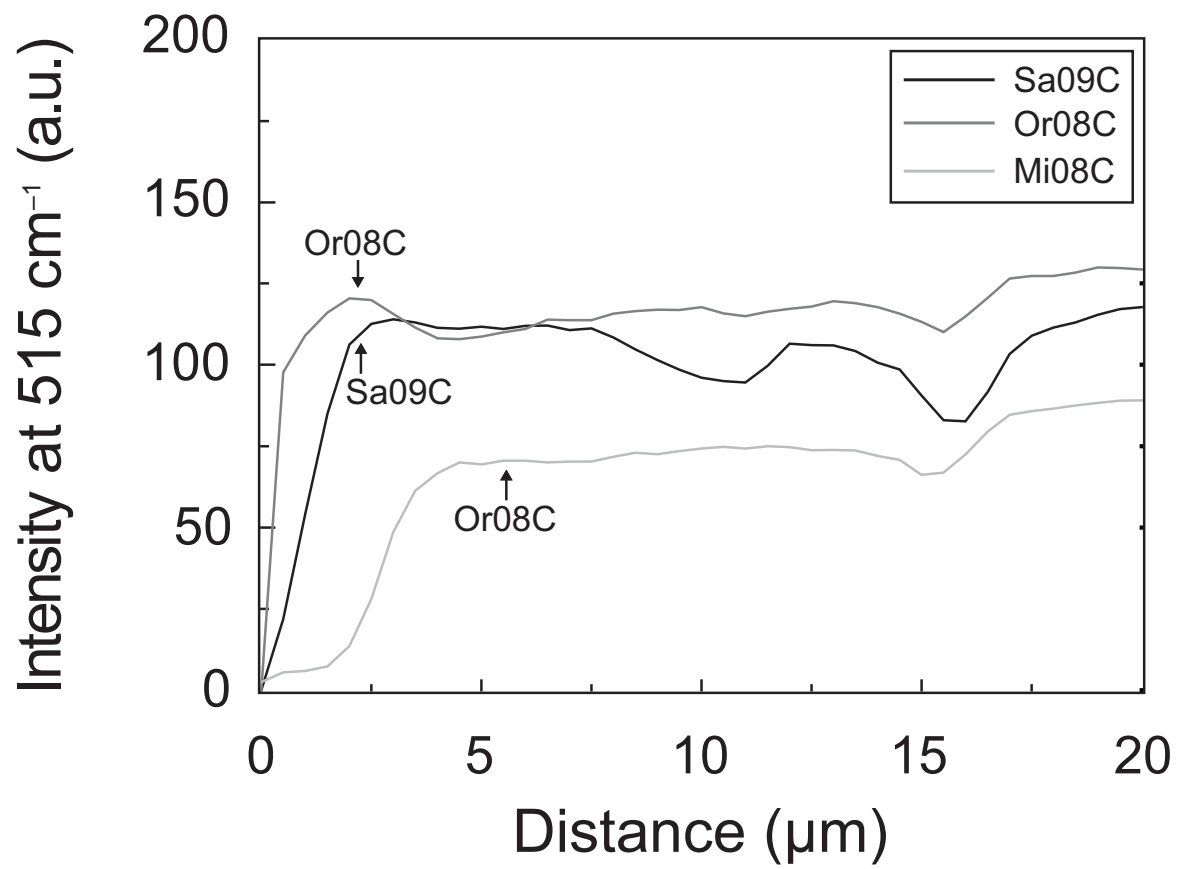


Figure 4

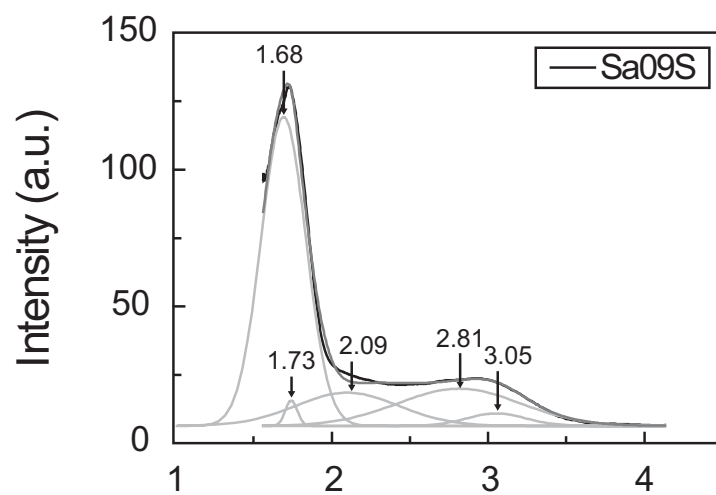
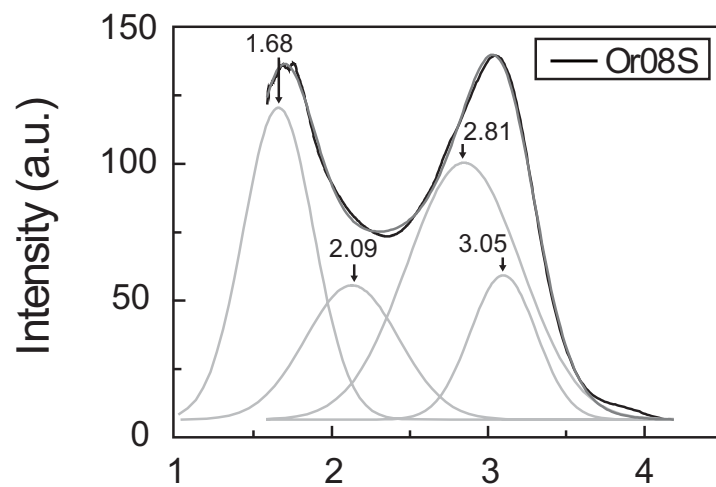
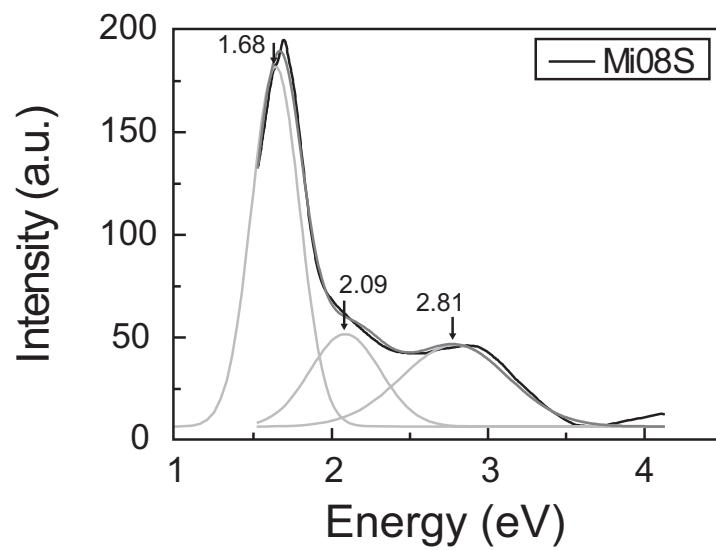
a**b****c**

Figure 5

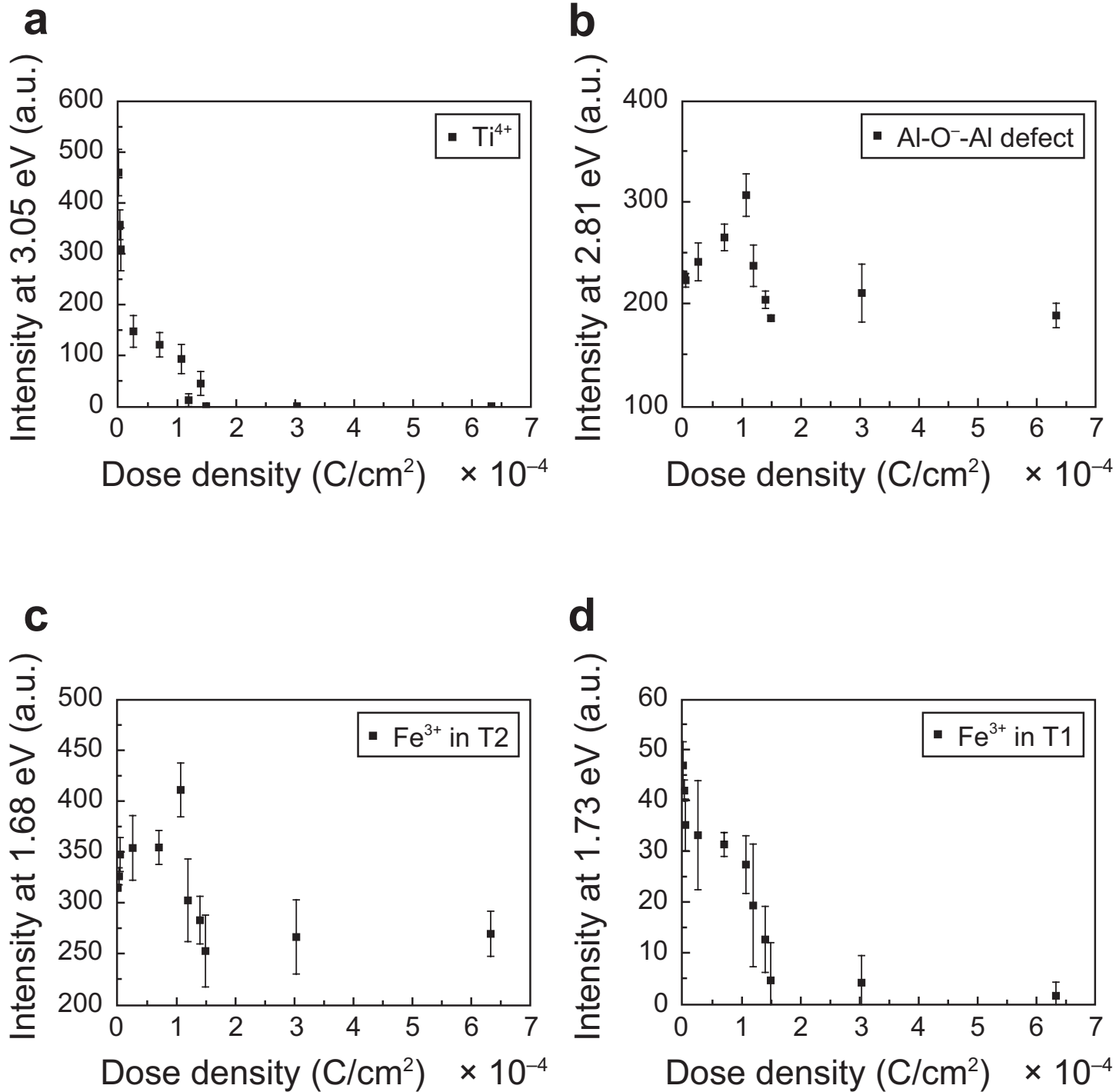


Figure 6

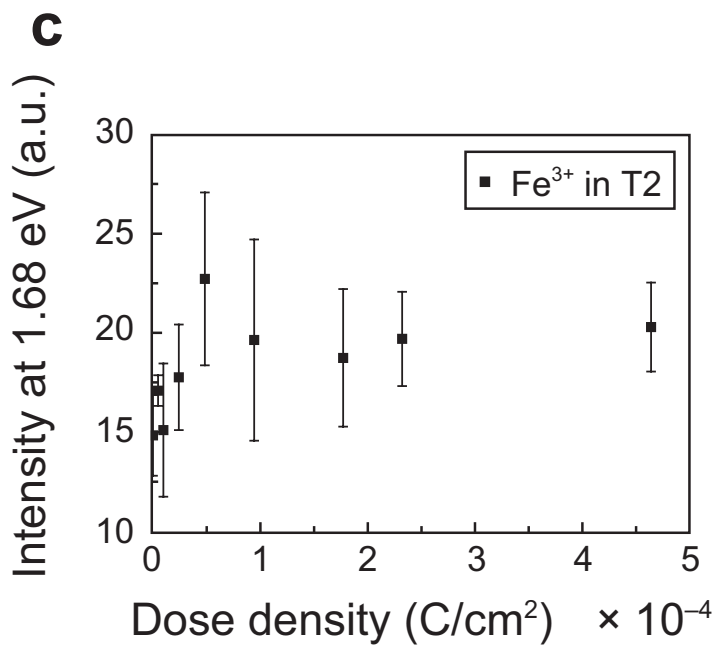
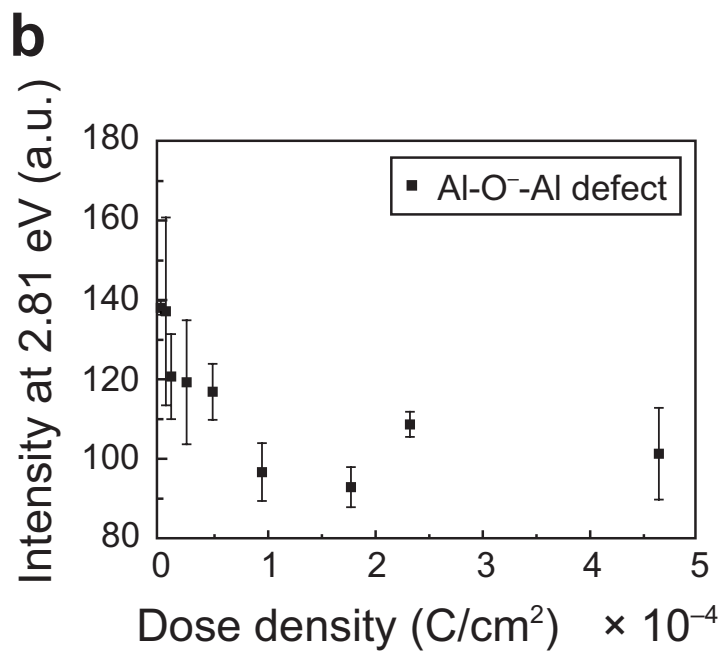
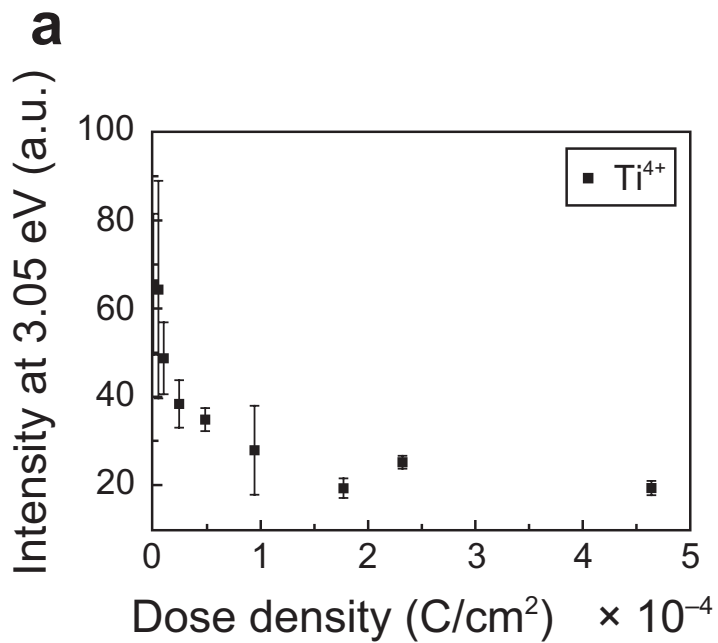


Figure 7

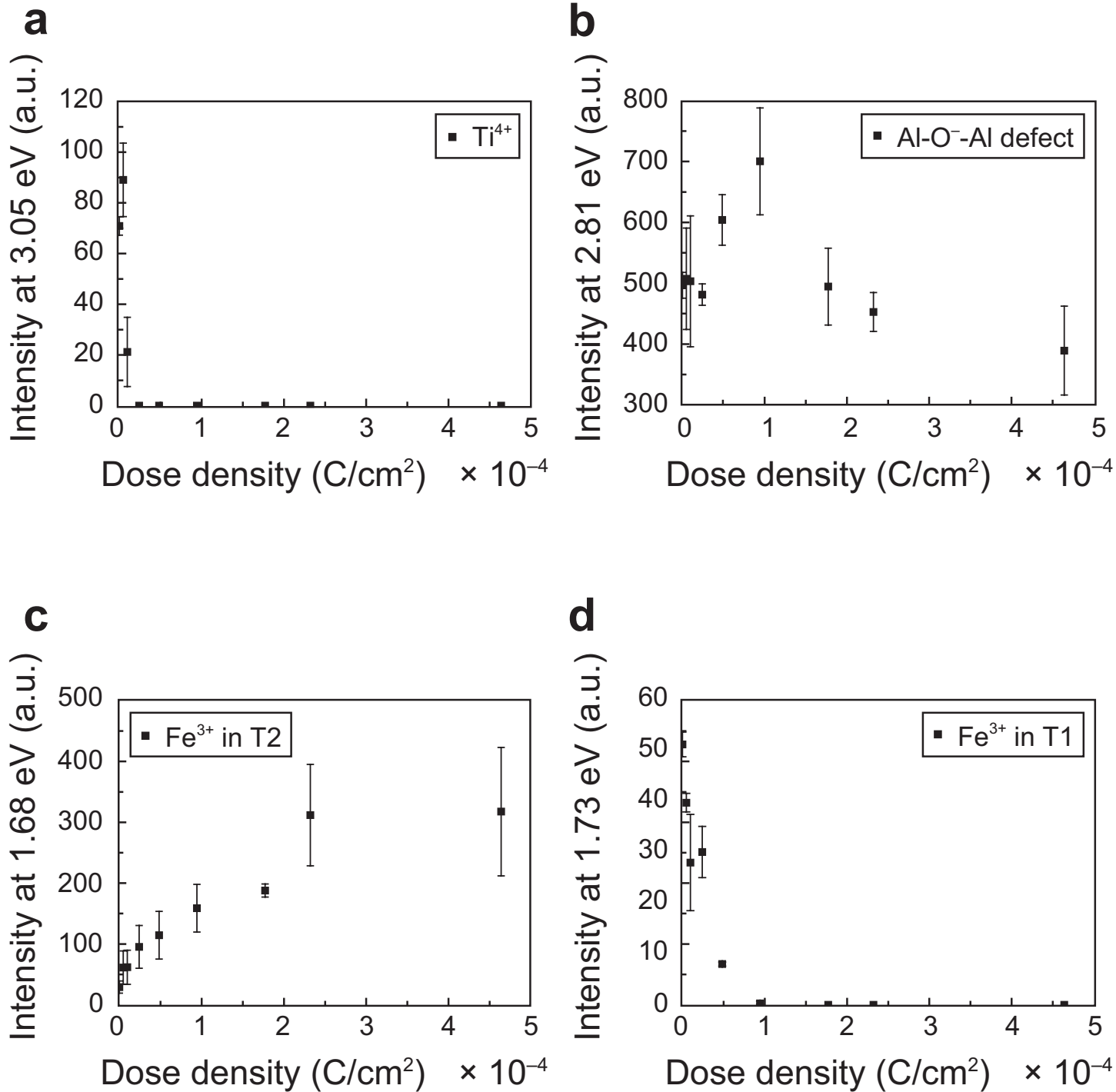


Figure 8

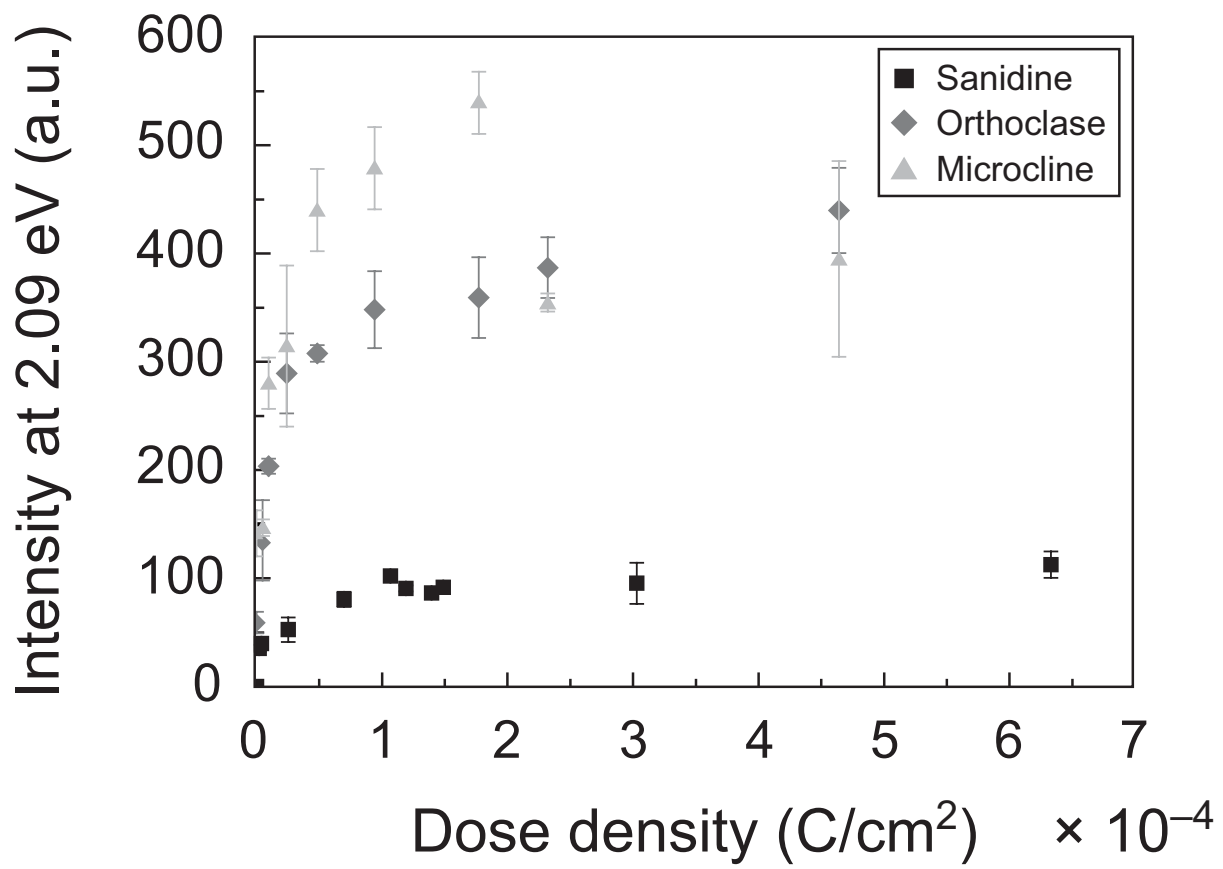


Figure 9